

## Article

# Highly Efficient CeO<sub>2</sub>–CuCrO<sub>2</sub> Composite Nanofibers Used for Electrochemical Detection of Dopamine in Biomedical Applications

Heng-Jyun Lei<sup>1,2</sup>, Homg-Ming Su<sup>1,2</sup>, Dhanapal Vasu<sup>1,2</sup>, Yu-Feng You<sup>1,2</sup>, Te-Wei Chiu<sup>1,2,\*</sup>  
and Naratip Vittayakorn<sup>3,\*</sup>

<sup>1</sup> Department of Materials and Mineral Resources Engineering, National Taipei University of Technology, 1, Section 3, Taipei 106, Taiwan; leijeffer00@gmail.com (H.-J.L.); b22775411@gmail.com (H.-M.S.); dvasukalyan@gmail.com (D.V.); t110788013@ntut.org.tw (Y.-F.Y.)

<sup>2</sup> Institute of Materials Science and Engineering, National Taipei University of Technology, No. 1, Section 3, Taipei 106, Taiwan

<sup>3</sup> Advanced Materials Research Unit, School of Science, King Mongkut's Institute of Technology Lad Krabang, Bangkok 10520, Thailand

\* Correspondence: tewei@ntut.edu.tw (T.-W.C.); naratip.vi@kmitl.ac.th (N.V.)

**Abstract:** Dopamine (DA) plays a crucial role in the functioning of the human central nervous system, participating in both physiological and psychological processes. It is an important research topic in biomedical science. However, we need to constantly monitor the concentration of dopamine in the body, and the sensors required for this usually require good sensitivity in order to achieve fast and accurate measurements. In this research project, a CeO<sub>2</sub> and CuCrO<sub>2</sub> composite nanofiber was prepared for the electrochemical detection of dopamine. Coaxial electrospinning techniques were used to prepare CeO<sub>2</sub>–CuCrO<sub>2</sub> composite nanofibers. The characterization techniques of X-ray diffractometer (XRD), Raman, and X-ray photoelectron spectroscopy (XPS) were used to analyze the composite's crystal structure, vibrational bonds, and elemental composition, while SEM and TEM were used to analyze the composite's surface structure, morphology, and microstructure. The prepared nanofiber outer layer was found to have an average thickness of 70.96 nm, average fiber diameter of 192.49 nm, and an average grain size of about ~12.5 nm. The BET analysis was applied to obtain the specific surface area (25.03 m<sup>2</sup>/gm). The proposed nanofiber-decorated disposable screen-printed carbon electrode acted as a better electrochemical sensor for the detection of dopamine. Moreover, the electrocatalyst had a better limit of detection, 36 nM with a linear range of 10 to 100 μM, and its sensitivity was 6.731 μA μM<sup>-1</sup> cm<sup>-2</sup>. In addition, the proposed electrocatalyst was successfully applied to real-time potential applications, namely, to the analysis of human urine samples in order to obtain better recovery results.

**Keywords:** CeO<sub>2</sub>; CuCrO<sub>2</sub> nanofibers; coaxial electrospinning; dopamine sensor; morphology control



**Citation:** Lei, H.-J.; Su, H.-M.; Vasu, D.; You, Y.-F.; Chiu, T.-W.; Vittayakorn, N. Highly Efficient CeO<sub>2</sub>–CuCrO<sub>2</sub> Composite Nanofibers Used for Electrochemical Detection of Dopamine in Biomedical Applications. *Fibers* **2023**, *11*, 66. <https://doi.org/10.3390/fib11080066>

Academic Editor: Alexandru Mihai Grumezescu

Received: 2 May 2023

Revised: 4 July 2023

Accepted: 17 July 2023

Published: 25 July 2023



**Copyright:** © 2023 by the authors. Licensee MDPI, Basel, Switzerland. This article is an open access article distributed under the terms and conditions of the Creative Commons Attribution (CC BY) license (<https://creativecommons.org/licenses/by/4.0/>).

## 1. Introduction

One significant neurotransmitter is dopamine (DA), which regulates or coordinates cognition and emotions in the human body. Moreover, DA is the most important catecholamine that is present in the mammalian central nervous system. It regulates various physiological and cognitive functions, including emotion, movement, learning, and memory. The average levels of DA in human serum and blood are assessed to be in the range of 10<sup>-6</sup> to 10<sup>-9</sup> mol/L. When the DA concentrations are varied, which means that abnormal concentrations of DA are present, the imbalance is associated with serious diseases, such as Alzheimer's and Parkinson's [1–3]. In addition, the excessive consumption of caffeinated beverages or drug abuse can also lead to dopamine excess [4]. Therefore, studying the levels and distribution of dopamine in the human body is of great significance in the field

of biomedicine. Electrochemical and wearable sensors have attracted significant attention due to their advantages of real-time detection. Currently, wearables are not available for functions beyond generally tracking the indicators of bodily motion, respiration rate, and electrocardiogram-based metrics, and are unable to provide information at smaller-scale levels. To overcome this limitation and advance the rapid development of wearable electrochemical sensors, science is developing a new avenue via which to sense analytes. Among the various types of biofluids, it is very difficult to obtain the non-invasive monitoring of biological samples [5–10].

Delafossite-based materials [3] are gradually receiving attention in the field of biomedicine. In terms of dopamine sensors, copper-based materials are a promising choice because of their excellent conductivity [11,12], biocompatibility [13–15], and excellent chemical stability [16,17]. Among the delafossite materials,  $\text{CuCrO}_2$  has attracted much attention in the field of semiconductors and solar cells due to its unique properties [17,18]. In addition, modifying the surface of delafossite materials can also improve their selectivity and sensitivity [19–21], thereby improving their chemical properties.

Rare-earth metal oxides have been extensively used in various applications due to their high activity, excellent redox ability, low toxicity, and high mechanical and thermal stability [21,22]. Moreover,  $\text{CeO}_2$  exhibits an outstanding oxygen storage capacity [23], reduction ability [24], and chemical- and photostability among the other rare-earth metals [25]. The valence state of Ce can switch between Ce(III) and Ce(IV), which contributes to the generation of electron–hole pairs [17,26,27]. Furthermore,  $\text{CeO}_2$  can absorb photons in the UV and visible light ranges to generate electron–hole pairs [28–30], which enhances its applications.

Based on the literature studies, this article reports upon the preparation of  $\text{CeO}_2$ – $\text{CuCrO}_2$  composite nanofibers using coaxial electrospinning technology, fibers in which  $\text{CeO}_2$  serves as the outer layer and  $\text{CuCrO}_2$  serves as the inner layer. The morphology of the nanofibers is controlled by adjusting the voltage and the concentration of the precursor solution. The composite nanofibers can be used as an electrocatalyst for dopamine sensing. The prepared  $\text{CeO}_2$ – $\text{CuCrO}_2$  nanofibers are analyzed via various characterization techniques.

## 2. Experimental

### 2.1. Materials

Polyvinylpyrrolidone (PVP, ACROS, purity: 85–95%), cerium nitrate hexahydrate (Alfa Aesar, Ward Hill, MA, United States, purity: 99.5%),  $\text{Cu}(\text{NO}_3)_2 \cdot 3\text{H}_2\text{O}$  (Showa, Amsterdam, The Netherlands, purity: 99.0%),  $\text{Cr}(\text{NO}_3)_3 \cdot 9\text{H}_2\text{O}$  (ACROS, Geel, Belgium, purity: 98.5%), and dimethylformamide (DMF, Showa, purity: 99.8%) were used.

### 2.2. Preparation of $\text{CeO}_2$ – $\text{CuCrO}_2$ Composite Nanofibers

The coaxial needles setup is different from that of the general electrospinning setup. The two precursor solutions need to be separately loaded into different syringes before being connected to the coaxial needle. The working distance (distance between the needle and collection platform), temperature and humidity need to be adjusted appropriately before the experimental process. The  $\text{CeO}_2$  and  $\text{CuCrO}_2$  solution flow rates are  $0.04 \text{ mL h}^{-1}$  and  $0.02 \text{ mL h}^{-1}$ , respectively. The chamber temperature is kept below  $40 \text{ }^\circ\text{C}$  and the humidity is below 25%. As shown in Figures 1 and 2, the applied voltage is controlled by a power supply; subsequently, the high voltage is applied to the droplet, and static electricity accumulates on the droplet. When the voltage exceeds the threshold, the liquid ruptures and sprays droplets from a flow-out point, and the droplets are pulled and elongated into fibers by the electrostatic repulsive force. Finally, the initial spun fibers are obtained on the collection net. Then, the prepared nanofiber is annealed using an air atmosphere with a vacuum of 1.1 torr. The annealing process is a two-step process using different temperatures ( $500$  and  $600 \text{ }^\circ\text{C}$ ), with a ramping rate of  $1 \text{ }^\circ\text{C}$  per minute. The first annealing process is applied to remove the PVP compounds. The second step of the annealing process

is applied in order to obtain the pure phase of  $\text{CeO}_2\text{-CuCrO}_2$  [29]. Moreover, the  $\text{CeO}_2$  and  $\text{CuCrO}_2$  solution preparation methods are mentioned in the Supplementary Information.

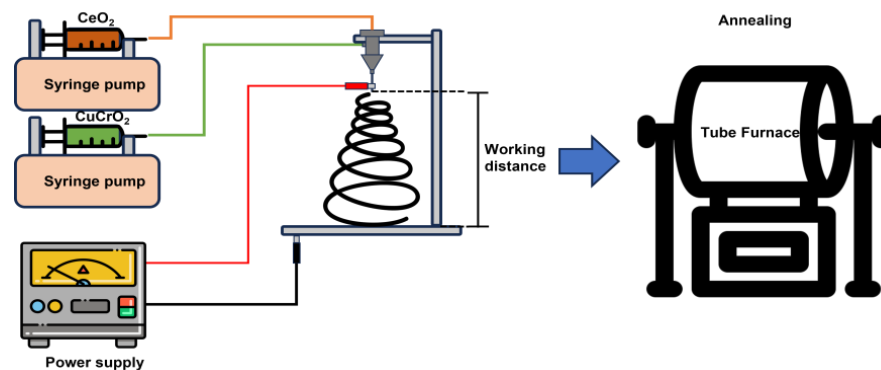


Figure 1. Schematic diagram for nanofiber preparation.

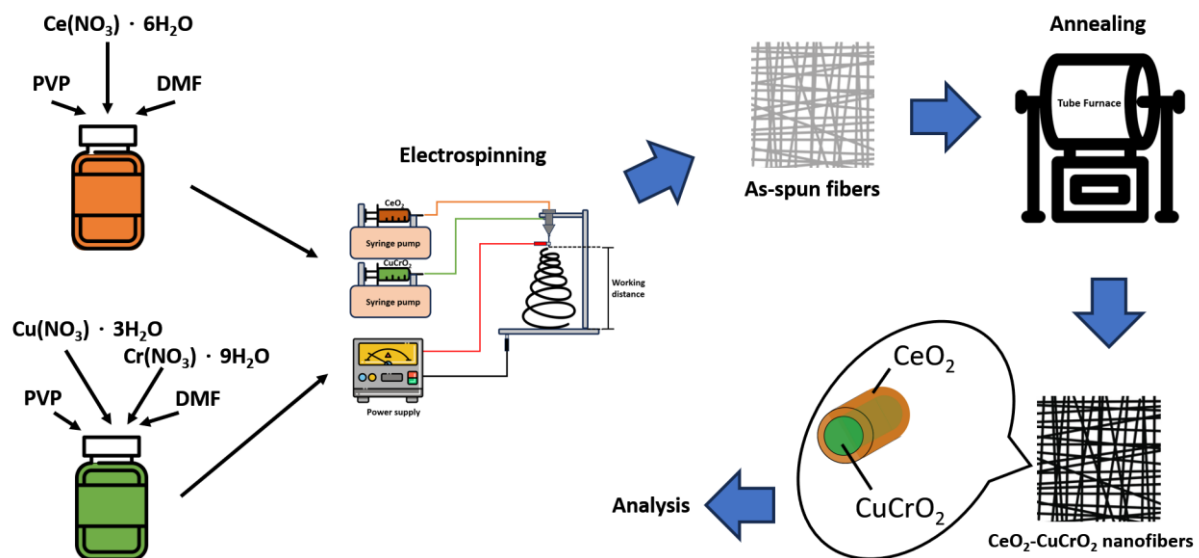


Figure 2. Schematic diagram of experimental setup.

### 3. Results and Analysis

#### 3.1. XRD Analysis

The crystallinity of the  $\text{CeO}_2\text{-CuCrO}_2$  composite nanofibers was analyzed via XRD techniques, as shown in Figure 3. The different concentrations of the  $\text{CeO}_2\text{-CuCrO}_2$  composite nanofiber diffraction patterns are presented in Figure 3 for comparative studies only. The figure shows that the diffraction patterns of (111), (200), (220), (311), and (222) related to  $\text{CeO}_2$  were presented at  $28.5^\circ$ ,  $33.0^\circ$ ,  $47.5^\circ$ ,  $56.3^\circ$ , and  $59.0^\circ$ , respectively. Moreover, the peaks related to  $\text{CuCrO}_2$  also obtained at  $31.4^\circ$ ,  $36.4^\circ$ , and  $40.9^\circ$  corresponded to the (006), (012), and (104) planes, respectively. The peaks related to  $\text{CeO}_2$  increased when the concentration of  $\text{CeO}_2$  increased. Moreover, the crystalline peak intensity increased, while a concentration of 0.2:0.1 M (Ce:CuCr) with a higher full-width half maximum was obtained. In addition, the crystallite size of the prepared nanofibers was evaluated using the Debye–Scherrer equation ( $D = k\lambda/\beta\cos\theta$ ) and their micro-strain was determined using the Williamson–Hall method. These basic parameter values are reported in Table 1 [31,32]. For the XRD result, a better crystalline structure and surface morphology (see SEM and TEM images) was observed at a 0.2:0.1 M concentration of  $\text{CeO}_2$  and  $\text{CuCrO}_2$ , respectively. Hence, we have used these materials for further characterizations and applications.

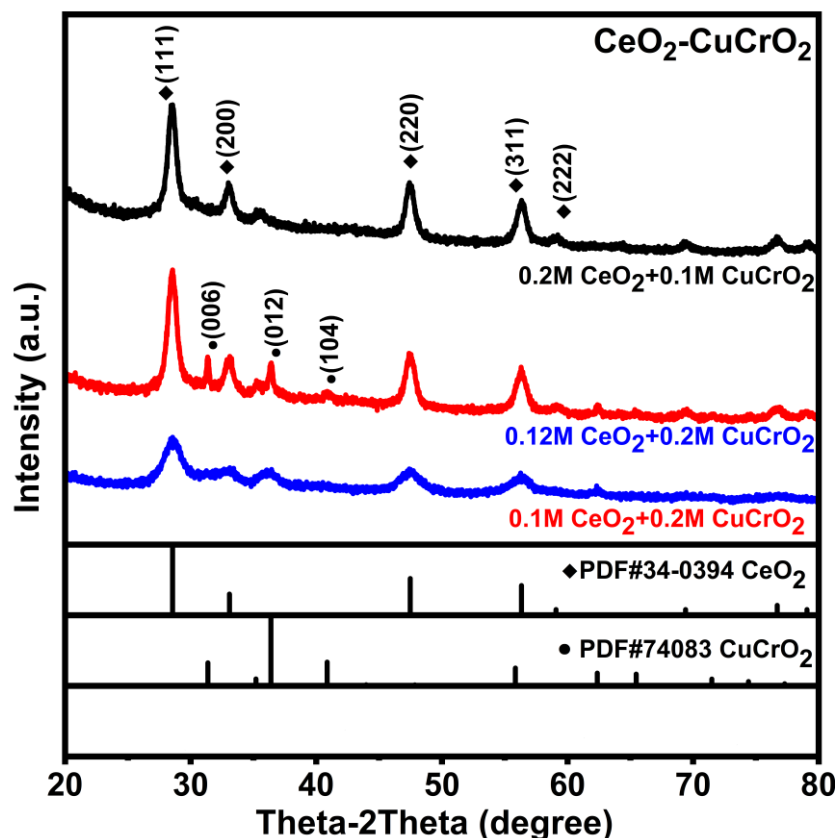


Figure 3. XRD pattern of CeO<sub>2</sub>-CuCrO<sub>2</sub>.

Table 1. The prepared samples’ average crystallite size, micro-strain, and FWHM.

Sample Name	Material	Crystalline Size (nm)	Micro-Strain (10 <sup>3</sup> )	FWHM
CCC1:2	CuCrO <sub>2</sub>	28.02	4.40	0.33
	CeO <sub>2</sub>	5.20	21.85	1.85
CCC1.2:2	CuCrO <sub>2</sub>	7.11	17.80	1.30
	CeO <sub>2</sub>	9.86	11.27	0.97
CCC2:1	CuCrO <sub>2</sub>	5.63	20.32	1.70
	CeO <sub>2</sub>	10.69	10.48	0.90

### 3.2. Raman Analysis

The vibrational bonds of the nanofibers were studied using Raman techniques. The nanofibers’ vibrational bonds are shown in Figure 4. In Figure 4, it is indicated that the nanofibers had four active vibrational modes of Eu, Ag, Eg, and A1g, which were observed at 136 cm<sup>-1</sup>, 230 cm<sup>-1</sup>, 484 cm<sup>-1</sup>, and 720 cm<sup>-1</sup>, respectively. These modes were presented due to the lattice vibration modes generated by CuCrO<sub>2</sub> and CeO<sub>2</sub> [33,34]. However, these peaks are actually red-shifted, based on the previously reported one [35,36], which occurred to the influence of defect impurities on the vibration frequency, leading to an increase in the wavelength.

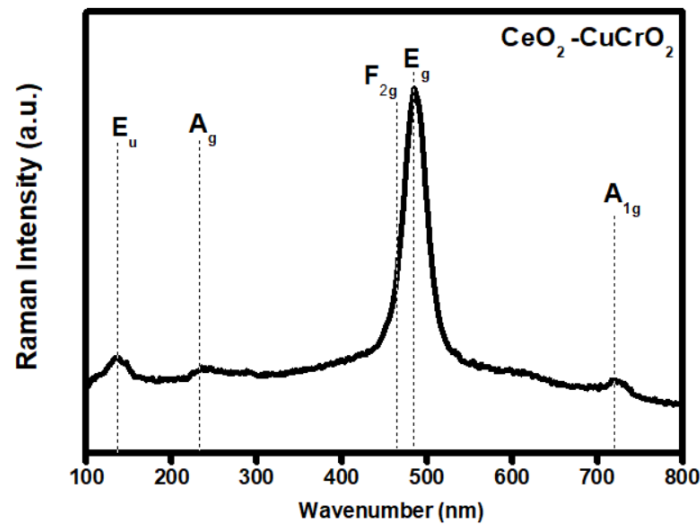


Figure 4. Raman spectrum of  $\text{CeO}_2\text{-CuCrO}_2(2:1)$  composite nanofibers under the excitation line of 532 nm.

### 3.3. X-ray Photoelectron Spectroscopy (XPS)

An evaluation of the chemical composition of the annealed CCC2:1 nanofiber was performed using XPS. The XPS high-resolution spectra for all elements are presented in Figure 5. The Cu core-level deconvoluted spectra are shown in Figure 5a, indicating that Cu 2p had a doublet of Cu  $2p_{1/2}$  and Cu  $2p_{3/2}$ . The  $\text{Cu}^+$  and  $\text{Cu}^{2+}$  oxidation states related to Cu  $2p_{3/2}$  were presented at  $932\text{ cm}^{-1}$  and  $936\text{ cm}^{-1}$ , respectively. Meanwhile, the  $\text{Cu}^+$  and  $\text{Cu}^{2+}$  oxidation states related to Cu  $2p_{1/2}$  were presented at  $952\text{ cm}^{-1}$  and  $956\text{ cm}^{-1}$ , respectively. Moreover, the satellite peak also presented at  $938$  and  $948\text{ cm}^{-1}$  was due to the incomplete transformation of the Cu valence state [37]. Figure 5b shows the Cr core-level deconvoluted spectra. The Cr deconvoluted into two main peaks of Cr  $2p_{3/2}$  and Cr  $2p_{1/2}$ , respectively. Moreover, these two spin-orbit splits had different  $\text{Cr}^{3+}$  and  $\text{Cr}^{6+}$  oxidation states that were presented at  $576\text{ cm}^{-1}$ ,  $579\text{ cm}^{-1}$ ,  $587\text{ cm}^{-1}$  and  $589\text{ cm}^{-1}$ , respectively [37]. The Ce core-level spectra are shown in Figure 5c. Figure 5c depicts the characteristic peaks of Ce  $3d_{5/2}$  that were presented in the range of  $882\text{--}900\text{ cm}^{-1}$  and the Ce  $3d_{3/2}$  presented in the range of  $900\text{--}908\text{ cm}^{-1}$  [38]. Moreover, the characteristic peaks of  $\text{O}_{1s}$  were also presented at around  $529\text{ cm}^{-1}$ ,  $531\text{ cm}^{-1}$ ,  $533\text{ cm}^{-1}$ ,  $534\text{ cm}^{-1}$ , and  $529\text{ cm}^{-1}$ , respectively. The peak at  $529\text{ cm}^{-1}$  was related to the lattice oxygen in  $\text{CeO}_2$ . The peaks at  $531\text{ cm}^{-1}$  and  $533\text{ cm}^{-1}$  were attributed to hydroxyl and water molecules, which may have been due to lattice vacancies and oxygen-deficient regions in the  $\text{CeO}_2$  matrix [37,38].

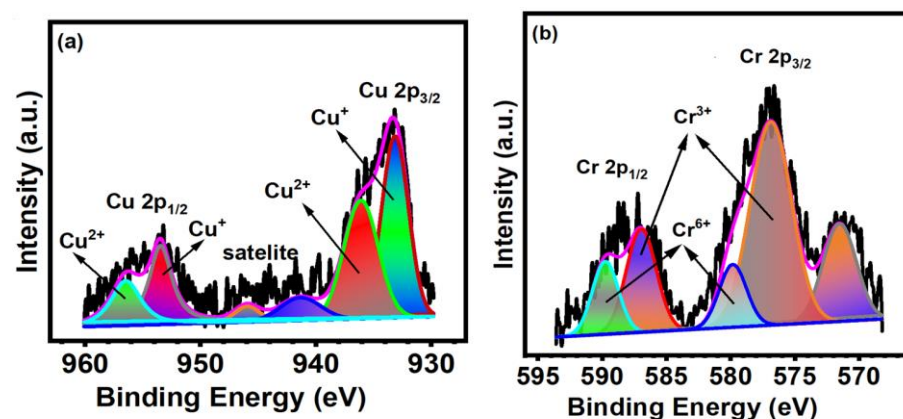
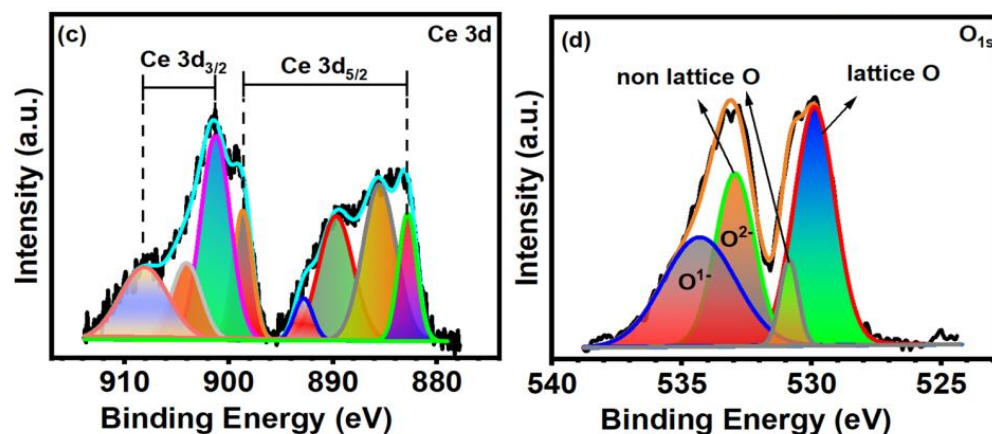


Figure 5. Cont.



**Figure 5.** XPS spectra for (a) Cu, (b) Cr, (c) Ce and (d) O spectra of CeO<sub>2</sub>–CuCrO<sub>2</sub>(2:1) composite nanofibers.

### 3.4. Surface Morphology and Topography Analysis

SEM analysis was used in order to evaluate the structure and surface morphology of the prepared materials. Figure 6 shows that the prepared materials had a tubular structure, which means that the particles successfully formed a fiber-like structure with a porous nature.

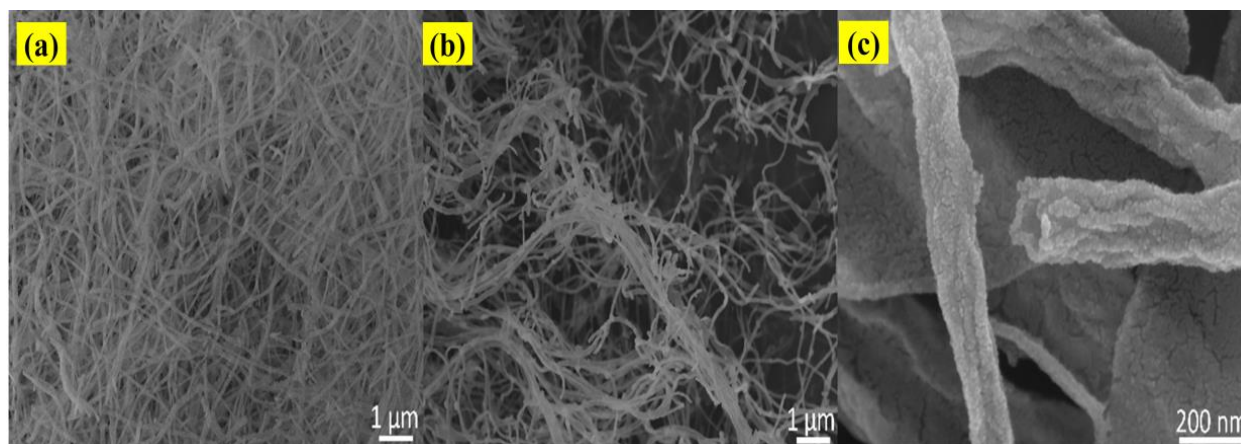


**Figure 6.** (a) SEM image of CeO<sub>2</sub>–CuCrO<sub>2</sub> composite nanofibers prepared with 24 kV, (b) CeO<sub>2</sub>–CuCrO<sub>2</sub> composite nanofibers' different positions, and (c) 200 nm scale for CeO<sub>2</sub>–CuCrO<sub>2</sub> composite nanofibers.

TEM analysis was used in order to obtain the morphology and topography of the nanofibers, as shown in Figure 7 with different magnifications. The TEM images clearly indicated that the fibers had a thick wall with a porous nature. Meanwhile, the tube wall exhibited small dark particles or spots that formed due to the dispersion of metal nanoparticles. In order to determine the distribution of elements over the nanofibers, EDS analysis was performed. The EDS analysis provided confirmation of all the elements present in the prepared nanofiber. The EDS mapping of the CeO<sub>2</sub>–CuCrO<sub>2</sub> nanofiber is shown in Figure 7e–j. The copper, chromium, cerium and oxygen elements are evenly present, as observed from the EDS mapping. It confirms the composition of prepared CeO<sub>2</sub>–CuCrO<sub>2</sub> nanofibers by using different color coding.

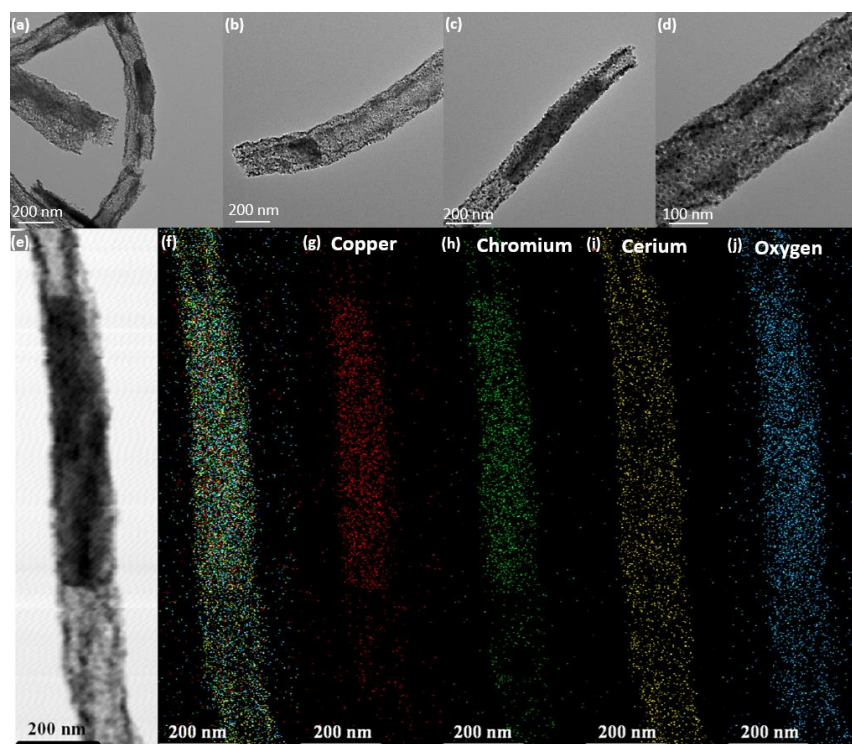


**Figure 7.** (a–e) TEM image of the  $\text{CeO}_2\text{-CuCrO}_2$  composite nanofibers prepared with 24 kV, whose annealing rate is  $3\text{ }^\circ\text{C}/\text{min}$ , (f) EDX analysis color mapping for all elements, and color mapping for (g) copper, (h) chromium, (i) cerium, and (j) oxygen.

### 3.5. BET Analysis

The porous nature and surface area of the nanofibers were measured by using BET analysis. The  $\text{CeO}_2\text{-CuCrO}_2$  composite had a better surface area of  $25.03\text{ m}^2/\text{g}$ . Comparing pure  $\text{CuCrO}_2$  [19],  $\text{CeO}_2$  [39], and  $\text{CeO}_2\text{-CuCrO}_2$  [17], prepared via the electrospinning and glycine combustion method, the specific surface area of the composite nanofibers obtained in this experiment was higher than that of  $\text{CuCrO}_2$  but much lower than that of the porous structured powders obtained via the  $\text{CeO}_2$  and glycine combustion method. However, this also proves that the combination of  $\text{CeO}_2$  and  $\text{CuCrO}_2$  improved the specific surface area (Table 2).

**Table 2.** Comparison of specific surface area.

Compound	Surface Area	Reference
$\text{CuCrO}_2$ (Electrospinning)	$7.85\text{ m}^2/\text{g}$	19
$\text{CeO}_2$ (Electrospinning)	$195.75\text{ m}^2/\text{g}$	39
$\text{CeO}_2\text{-CuCrO}_2$ (Combustion glycine nitrate)	$46.13\text{ m}^2/\text{g}$	17
$\text{CeO}_2\text{-CuCrO}_2$ (Electrospinning)	$25.03\text{ m}^2/\text{g}$	This work

## 4. Electrochemical Applications

### 4.1. The Electrochemical Ability of $\text{CeO}_2\text{-CuCrO}_2$ Composite Nanofibers to Detect Dopamine

The electrochemical properties of the bare electrode and  $\text{CeO}_2\text{-CuCrO}_2$  were tested for the detection of dopamine by using cyclic voltammetry. The electrochemical process was analyzed in the presence of a  $0.05\text{ M}$  PBS solution with  $20\text{ }\mu\text{M}$  of dopamine at a fixed scan rate of  $50\text{ mV}/\text{s}$ . Figure 8 shows the electrochemical ability of the  $\text{CeO}_2\text{-CuCrO}_2$  composite to detect dopamine. The bare or undecorated disposable SPCE showed a weak peak current. However, the nanofiber-decorated disposable SPCE had a higher peak current, which is presented in Figure 8b. This possibly occurred due to the nanofibers' structure, morphology, porosity and conductivity. Moreover, the prepared materials had a higher active surface

area of  $0.106 \text{ cm}^2$ , which was obtained by using the Randles–Sevcik equation with the help of the ferric cyanide system (refer to the Supplementary Information). The tubular structure can provide a higher conductive behavior. As a result, the proposed nanofiber electrode is a potential candidate for DA detection due to its enormous electrochemical ability.

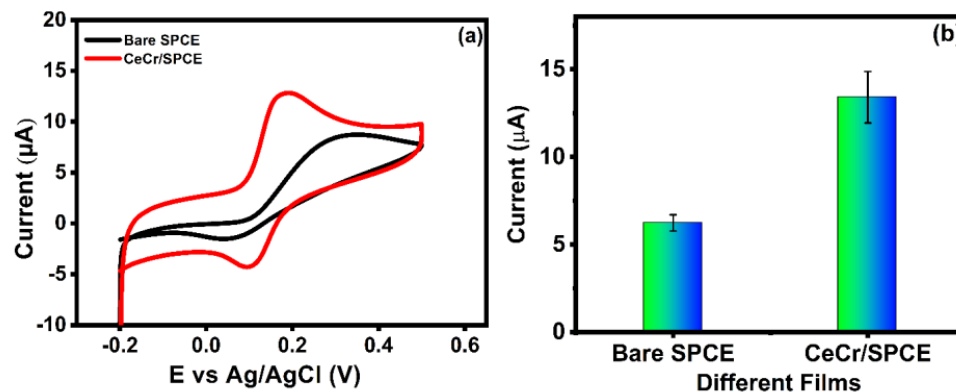


**Figure 8.** (a) CV curves for bare and decorated disposable SPCE; (b) bar graph expressing the current density values of the bare SPCE and  $\text{CeO}_2\text{-CuCrO}_2$ -decorated SPCE.

#### 4.2. Influence of pH

The oxidation of DA is strongly dependent on the electrolyte pH; this is an essential parameter used to optimize the pH for DA oxidation. The electrochemical ability of DA on the nanofiber composites was measured via CV in a PBS solution with varying pH levels, using a DA concentration of  $20 \mu\text{M}$  and a scan rate of  $50 \text{ mV/s}$ . As shown in Figure 9a, the peak current of DA varied and increased with respect to the solution's pH. A higher peak current was obtained at a neutral pH of 7.0. Meanwhile, the peak current density decreased when the pH was varied from neutral to acidic and from neutral to basic conditions. This may be attributed to DA molecules being protonated to  $\text{H}_3\text{DA}^+$ , which strongly reacts with the negatively charged ions on the surface of nanofibers such as  $^-\text{OH}$ ,  $^-\text{O}$  and  $^-\text{F}$  via electrostatic interactions [40–42]. Meanwhile, in acidic conditions, the  $\text{H}^+$  connects with  $\text{H}_3\text{DA}^+$  to react with the nanofiber, thus restricting the interaction of DA and the nanofibers. More notably, a lower pH condition is not conducive to the DA deprotonation process. Simultaneously, when the pH was higher, the DA molecules were unstable and could be oxidized to form quinone, resulting in a lower peak current. Furthermore, the peak potential was shifted [34].

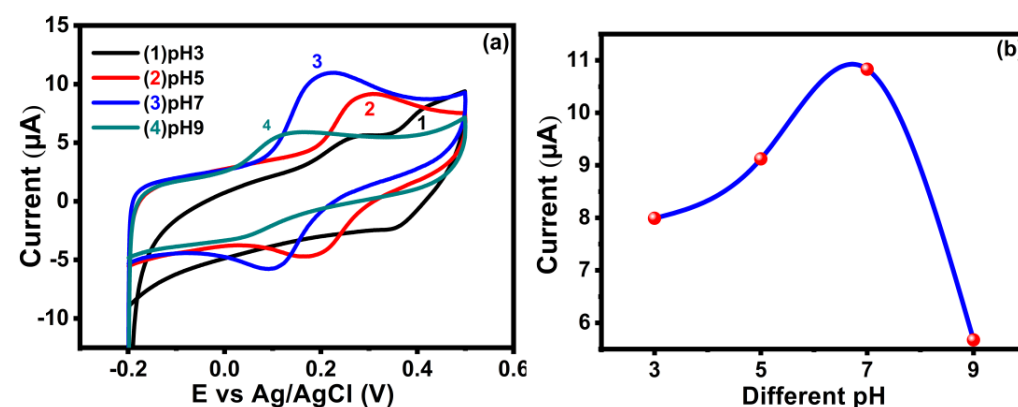


**Figure 9.** (a) Electrochemical activity of  $\text{CeO}_2\text{-CuCrO}_2$  at different pH levels, measured using cyclic voltammetry. (b) The trend in the current changes for different pH levels.

#### 4.3. Effect of Different Dopamine Concentrations on $\text{CeO}_2\text{-CuCrO}_2$ Composite Nanofibers Electrode

The electrochemical properties of CCC2:1 in aqueous solutions with different concentrations of DA were studied at a scan rate of  $50 \text{ mV/s}$ . An increase in the concentrations

(10–60  $\mu\text{M}$ ) of DA resulted in a steady increase in the peak current, as shown in Figure 10a. The rapid changes in the peak potential after adding DA indicated its excellent catalytic behavior facilitating the detection of DA [41,42], with the materials enhancing the oxidation and electron transfer rates. The linear regression plot of  $I_{\text{pa}}$  in Figure 10b fits very well with the correlation coefficient ( $R^2$ ) value of 0.996, indicating that the designed electrochemical sensor has sufficient electrochemical redox properties for DA detection.

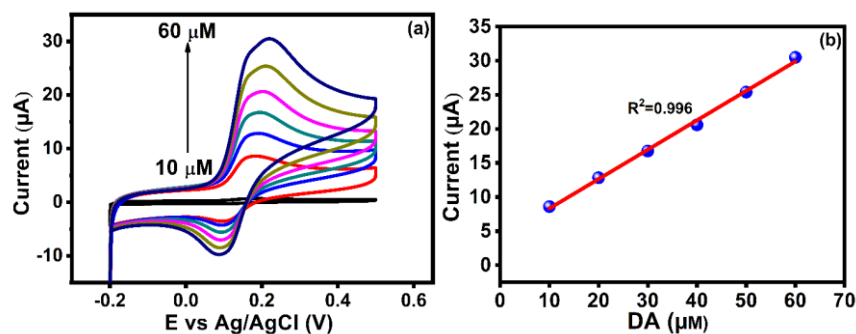


**Figure 10.** (a) Cyclic voltammetry curve displaying the electrocatalytic activity of CeO<sub>2</sub>-CuCrO<sub>2</sub> with the addition of different concentrations of DA aqueous solution at a rate of 50 mV/s. (b) Plot showing the current vs. the volume of the DA solution.

#### 4.4. Influence of Scan Rates on CeO<sub>2</sub>-CuCrO<sub>2</sub> Composite Nanofibers

Changes in the current of CCC1:2 were observed in a 30  $\mu\text{M}$  DA aqueous solution as the scan rate was increased from 20 mV/s to 200 mV/s. As shown in Figure 11a, there was almost no change in the peak potential, while the current increased with the increase in the scan rate. Figure 11b shows the trend between the current and scan rate, with an  $R^2$  value of 0.996. This result clearly indicates that the oxidation–reduction process of DA on the CCC2:1-modified electrode surface adsorbed the DA molecules. Hence, this process is a surface-controlled process [40,41].

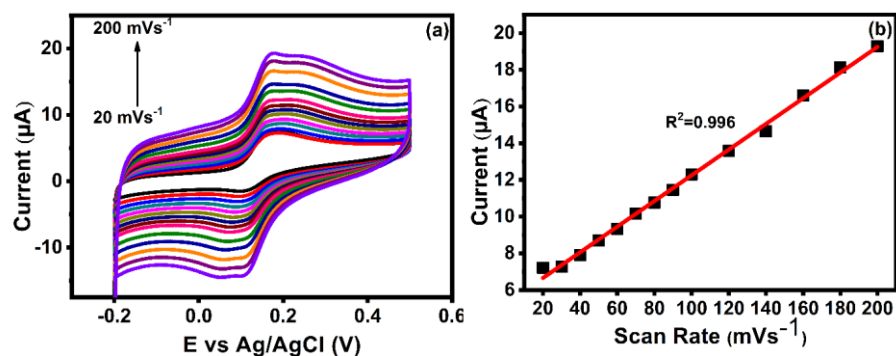


**Figure 11.** (a) Cyclic voltammetry curve displaying the electrocatalytic activity of the CeO<sub>2</sub>-CuCrO<sub>2</sub> composite with the addition of a 30  $\mu\text{M}$  aqueous solution of DA. (b) Plot showing the current vs. the scan rate.

#### 4.5. DA Detection Using DPV

Differential pulse voltammetry (DPV) is one of the most selective and sensitive techniques widely used for quantitative analysis in electrochemical detection. Figure 12a shows the DPV curves obtained on the surface of the CCC2:1 electrode with different concentrations of DA. The DA detection range is 0–100  $\mu\text{M}$ , and a linear relationship between the peak current and DA concentration can be observed, as shown in Figure 12b. The limit of detection (LoD) for DA detection using CCC2:1 in this experiment is approximately 36 nM, with a sensitivity of  $6.731 \mu\text{A} \mu\text{M}^{-1} \text{cm}^{-2}$ . Combining these results demonstrates that the

CeO<sub>2</sub>–CuCrO<sub>2</sub> composite nanofibers can be used as a DA sensor. The LoD was calculated using the following mathematical expressions [40–42]:

$$\text{LoD} = 3 \times \text{standard deviation (SD)}/\text{slope}$$

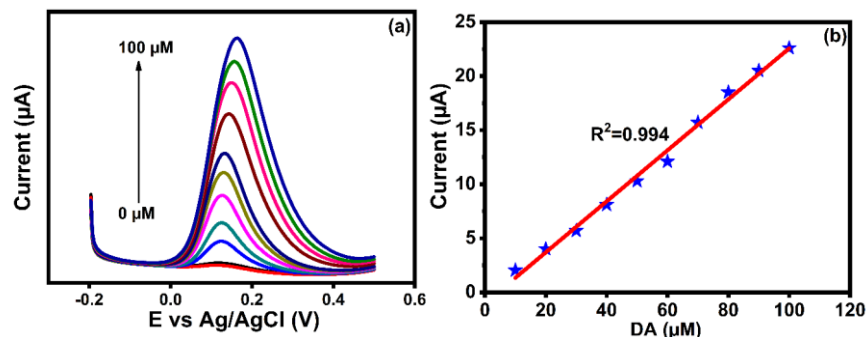


**Figure 12.** (a) DPV curves for different concentrations of DA and (b) the linear relationship between the concentration of DA added and the peak current.

#### 4.6. Real-Samples Analysis

The real-samples analysis data are reported in Table S2. The results indicating that the proposed nanofiber-decorated electrodes have a higher sensitivity, and a higher level of conductivity that is able to facilitate the detection of DA in biological samples for bio-medical applications. Finally, the proposed materials' stability, repeatability, and reproducibility studies are provided in the Supplementary Information (see Figure S2).

## 5. Conclusions

In conclusion, CeO<sub>2</sub>–CuCrO<sub>2</sub> nanofibers were successfully prepared using the coaxial electrospinning method at 24 kV. An evaluation of the basic material properties of the annealed fibers was carried out using XRD, Raman, and XPS, confirming the obtained product as expected. XRD analysis revealed that CuCrO<sub>2</sub> has a greater grain size compared to CeO<sub>2</sub>. Cyclic voltammetry showed that the composite nanofiber increased the electrode's conductivity, and different currents were obtained by changing the pH value; the highest current, of approximately 13.41 μA, was obtained at pH 7. Under varying dopamine concentrations, the current change of this material is proportional to the concentration, and the stable growth trend observed indicates that its excellent catalytic behavior facilitates the detection of dopamine. Moreover, when the scan rate is increased, the peak potential and current growth trend remain stable. The DPV analysis curve shows a linear relationship between the peak current and dopamine concentration, and the calculated limit of detection is approximately 36 nM. The above analysis results confirm the potential of CeO<sub>2</sub>–CuCrO<sub>2</sub> composite nanofibers to be used as a biosensor for dopamine.

**Supplementary Materials:** The following supporting information can be downloaded at: <https://www.mdpi.com/article/10.3390/fib11080066/s1>, Figure S1. (a) CV curve for ferricyanide system for bare SPCE and CeCr decorated SPCE with scan rate of 50 mV/s, (b) Related current values bar diagram, (c) different scan rates (20–260 mV/s), and (d) related current values for square root of scan rates. Figure S2. CeCr/SPCE (a) stability, (b) repeatability and (c) reproducibility. Table S1. DA detection in human urine samples.

**Author Contributions:** H.-J.L.: Data curation, Methodology, Formal analysis, Writing-original draft, H.-M.S.: Data curation, Formal analysis, Writing-original draft, D.V.: Conceptualization, Investigation, Validation, Writing-original draft, Y.-F.Y.: Formal analysis, Writing-original draft, T.-W.C.: Supervision, Funding acquisition, Investigation, validation, Writing—review, and editing, N.V.: validation, Investigation, Writing—review and editing. All authors have read and agreed to the published version of the manuscript.

**Funding:** This research work was supported by the Ministry of Science and Technology of Taiwan (MOST 110-2221-E-027-024), the National Science and Technology Council of Taiwan (NSTC 111-2221-E-027-104), and the National Taipei University of Technology—King Mongkut’s Institute of Technology Ladkrabang Joint Research Program (NTUT-KMITL-112-01).

**Informed Consent Statement:** Not applicable.

**Data Availability Statement:** Data are not available upon request due to privacy/ethical restrictions.

**Conflicts of Interest:** The authors declare no conflict of interest.

## References

1. Olguín, H.J.; Guzmán, D.C.; García, E.H.; Mejía, G.B. The Role of Dopamine and Its Dysfunction as a Consequence of Oxidative Stress. *Oxid. Med. Cell. Longev.* **2015**, *2016*, 9730467. [[CrossRef](#)]
2. Velez-Pardo, C.; Jimenez del Rio, M.; Ebinger, G.; Vauquelin, G. Manganese and copper promote the binding of dopamine to “serotonin binding proteins” in bovine frontal cortex. *Neurochem. Int.* **1995**, *26*, 615–622. [[CrossRef](#)] [[PubMed](#)]
3. Bisaglia, M.; Bubacco, L. Copper Ions and Parkinson’s Disease: Why Is Homeostasis So Relevant? *Biomolecules* **2020**, *10*, 195. [[CrossRef](#)] [[PubMed](#)]
4. Volkow, N.D.; Wang, G.-J.; Logan, J.; Alexoff, D.; Fowler, J.S.; Thanos, P.K.; Wong, C.; Casado, V.; Ferre, S.; Tomasi, D. Caffeine increases striatal dopamine D2/D3 receptor availability in the human brain. *Transl. Psychiatry* **2015**, *5*, e549. [[CrossRef](#)]
5. Ferlazzo, A.; Espro, C.; Iannazzo, D.; Bonavita, A.; Neri, G. Yttria-zirconia electrochemical sensor for the detection of tyrosine. *Mater. Today Commun.* **2023**, *35*, 106036. [[CrossRef](#)]
6. Xu, Z.; Qiao, X.; Tao, R.; Li, Y.; Zhao, S.; Cai, Y.; Luo, X. A wearable sensor based on multifunctional conductive hydrogel for simultaneous accurate pH and tyrosine monitoring in sweat. *Biosens. Bioelectron.* **2023**, *234*, 115360. [[CrossRef](#)]
7. Gan, A.W.; Seah, G.E.; Kwek, L.H.; Goh, S.S. Ion transfer voltammetry of amino acids with an all-solid-state ion-selective electrode for non-destructive phenylalanine sensing. *Electroanalysis* **2023**, *35*, e202200501. [[CrossRef](#)]
8. Ferlazzo, A.; Espro, C.; Iannazzo, D.; Neri, G. Determination of phenylalanine by a novel enzymatic PHD/SPE biosensor. *IEEE Trans. Instrum. Meas.* **2023**, *72*, 9508308. [[CrossRef](#)]
9. Diedkova, K.; Pogrebnyak, A.D.; Kyrylenko, S.; Smyrnova, K.; Buranich, V.V.; Horodek, P.; Zukowski, P.; Koltunowicz, T.N.; Galaszkiwicz, P.; Makashina, K.; et al. Polycaprolactone–MXene Nanofibrous Scaffolds for Tissue Engineering. *ACS Appl. Mater. Interfaces* **2023**, *15*, 14033–14047. [[CrossRef](#)]
10. Kyrylenko, S.; Kornienko, V.; Gogotsi, O.; Oleshko, O.; Kolesnyk, M.; Mishchenko, O.; Zahorodna, V.; Buranich, V.; Pogrebnyak, A.; Zozulia, Y.; et al. Bio-functionalization of electrospun polymeric nanofibers by Ti<sub>3</sub>C<sub>2</sub>T<sub>x</sub> MXene. In Proceedings of the 2020 IEEE 10th International Conference Nanomaterials: Applications & Properties (NAP), Sumy, Ukraine, 9–13 November 2020; IEEE: Piscataway, NJ, USA, 2023; p. 02BA10-1.
11. Narro-Ríos, J.S.; Garduño-Wilches, I.; Alarcón-Flores, G.; Ruiz-Rojas, C.A.; Gómez-Lizárraga, K.; Aguilar-Frutis, M. Spray pyrolysis synthesis of a semi-transparent p-CuCrO<sub>2</sub>/n-ZnO heterojunction: Structural, optical, and electrical properties. *Phys. B Condens. Matter* **2021**, *624*, 413426. [[CrossRef](#)]
12. Lee, E.H.; Kim, E.B.; Akhtar, M.S.; Ameen, S. Delafossite CuCrO<sub>2</sub> nanoparticles as possible electrode material for electrochemical supercapacitor. *Ceram. Int.* **2022**, *48*, 16667–16676. [[CrossRef](#)]
13. Cheng, W.; Li, C.; Zhou, C.; He, Y.; Wei, R.; Hu, L.; Song, W.; Zhu, X.; Sun, Y. Existence of bipolar resistive switching with self-rectifying behavior in a p-CuCrO<sub>2</sub>/n-Si heterostructure. *Thin Solid Films* **2022**, *762*, 139542. [[CrossRef](#)]
14. Erfan, N.A.; Barakat, N.A.M.; Muller-Borer, B.J. Preparation and characterization of β-lactoglobulin/poly(ethylene oxide) magnetic nanofibers for biomedical applications. *Colloids Surfaces A Physicochem. Eng. Asp.* **2019**, *576*, 63–72. [[CrossRef](#)]
15. Sanam, P.K.J.A.; Shah, M.; Pradyumn, P.P. Structure induced modification on thermoelectric and optical properties by Mg doping in CuCrO<sub>2</sub> nanocrystals. *Solid State Commun.* **2022**, *353*, 114855. [[CrossRef](#)]
16. Chen, C.Y.; Sakthinathan, S.; Yu, C.L.; Wang, C.C.; Chiu, T.W.; Han, Q. Preparation and characterization of delafossite CuCrO<sub>2</sub> film on flexible substrate. *Ceram. Int.* **2021**, *47*, 23234–23239. [[CrossRef](#)]
17. Lin, S.-Y.; Chiu, T.-W.; Dong, C. Preparation and characterization of CuCrO<sub>2</sub>–CeO<sub>2</sub> composite nanopowder by a self-combustion glycine nitrate process. *Ceram. Int.* **2017**, *43*, S639–S642. [[CrossRef](#)]
18. Yu, C.-L.; Lai, G.-T.; Sakthinathan, S.; Lin, C.-C.; Chiu, T.-W.; Liu, M.-C. Hydrogen generation from methanol steam reforming process of CuCrO<sub>2</sub>–CeO<sub>2</sub> nanopowders catalyst. *Mater. Sci. Eng. B* **2022**, *286*, 115989. [[CrossRef](#)]
19. Çetin, Ç.; Akyıldız, H. Production and characterization of CuCrO<sub>2</sub> nanofibers. *Mater. Chem. Phys.* **2016**, *170*, 138–144. [[CrossRef](#)]
20. Trevino, K.M.; Tautges, B.K.; Kapre, R.; Franco, F.C., Jr.; Or, V.W.; Balmond, E.I.; Shaw, J.T.; Garcia, J.; Louie, A.Y. Highly Sensitive and Selective Spiropyran-Based Sensor for Copper(II) Quantification. *ACS Omega* **2021**, *6*, 10776–10789. [[CrossRef](#)]
21. Serafin, J.; Llorca, J. Nanoshaped Cerium Oxide with Nickel as a Non-Noble Metal Catalyst for CO<sub>2</sub> Thermochemical Reactions. *SSRN Electron. J.* **2022**, *2*, 2926. [[CrossRef](#)]
22. Chen, W.P.; He, K.F.; Wang, Y.; Chan, H.L.W.; Yan, Z. Highly mobile and reactive state of hydrogen in metal oxide semiconductors at room temperature. *Sci. Rep.* **2013**, *3*, 3149. [[CrossRef](#)] [[PubMed](#)]

23. Gopal, C.B.; García-Melchor, M.; Lee, S.C.; Shi, Y.; Shavorskiy, A.; Monti, M.; Guan, Z.; Sinclair, R.; Bluhm, H.; Vojvodic, A.; et al. Equilibrium oxygen storage capacity of ultrathin  $\text{CeO}_2\text{-}\delta$  depends non-monotonically on large biaxial strain. *Nat. Commun.* **2017**, *8*, 15360. [[CrossRef](#)] [[PubMed](#)]
24. Kumari, M.; Singh, S.P.; Chinde, S.; Rahman, M.F.; Mahboob, M.; Grover, P. Toxicity Study of Cerium Oxide Nanoparticles in Human Neuroblastoma Cells. *Int. J. Toxicol.* **2014**, *33*, 86–97. [[CrossRef](#)] [[PubMed](#)]
25. Raudonyte-Svirbutaviciene, E.; Neagu, A.; Vickackaite, V.; Jasulaitiene, V.; Zarkov, A.; Tai, C.-W.; Katelnikovas, A. Two-step photochemical inorganic approach to the synthesis of Ag-CeO<sub>2</sub> nanoheterostructures and their photocatalytic activity on tributyltin degradation. *J. Photochem. Photobiol. A Chem.* **2018**, *351*, 29–41. [[CrossRef](#)]
26. Murali, A.; Sarswat, P.K.; Free, M.L. Minimizing electron-hole pair recombination through band-gap engineering in novel ZnO-CeO<sub>2</sub>-rGO ternary nanocomposite for photoelectrochemical and photocatalytic applications. *Environ. Sci. Pollut. Res.* **2020**, *27*, 25042–25056. [[CrossRef](#)]
27. Wang, Q.; Zhou, X.; Ji, S.; Li, S.; Gu, J.; Shen, L.; Liu, P.; Yin, J.; Xu, G.; Shi, W. Synthesis and photocatalysis of novel Z-scheme CeO<sub>2</sub>/Ag-AgVO<sub>3</sub> heterojunction nanofibers and their efficient antibacterial properties. *J. Environ. Chem. Eng.* **2021**, *9*, 106498. [[CrossRef](#)]
28. Sabzehmeidani, M.M.; Karimi, H.; Ghaedi, M. CeO<sub>2</sub> nanofibers-CdS nanostructures n-n junction with enhanced visible-light photocatalytic activity. *Arab. J. Chem.* **2020**, *13*, 7583–7597. [[CrossRef](#)]
29. Wang, C.-C.; Yu, C.-L.; Sakthinathan, S.; Chen, C.-Y.; Chiu, T.-W.; Fu, Y.-S. Preparation and characterization of CuCrO<sub>2</sub>-CeO<sub>2</sub> nanofibers by electrospinning method. *J. Mater. Sci. Mater. Electron.* **2021**, *33*, 1091–1100. [[CrossRef](#)]
30. Lin, Y.-H.; Chiu, T.-W.; Park, J.-H. Lamination of CuCrO<sub>2</sub> thin films to poly methyl methacrylate substrate with boron nitride demolding layer. *Ceram. Int.* **2018**, *44*, S22–S25. [[CrossRef](#)]
31. Dong, Y.; Lin, H.; Qu, F. Synthesis of ferromagnetic ordered mesoporous carbons for bulky dye molecules adsorption. *Chem. Eng. J.* **2012**, *193–194*, 169–177. [[CrossRef](#)]
32. Saravanan, S.; Carolin, C.F.; Kumar, P.S.; Chitra, B.; Rangasamy, G. Biodegradation of textile dye Rhodamine-B by *Brevundimonas diminuta* and screening of their breakdown metabolites. *Chemosphere* **2022**, *308*, 136266. [[CrossRef](#)]
33. Aktas, O.; Truong, K.D.; Otani, T.; Balakrishnan, G.; Clouter, M.J.; Kimura, T.; Quirion, G. Raman scattering study of delafossite magnetoelectric multiferroic compounds: CuFeO<sub>2</sub> and CuCrO<sub>2</sub>. *J. Physics Condens. Matter* **2011**, *24*, 036003. [[CrossRef](#)]
34. Monteiro, J.F.H.L.; Siqueira, E.C.; Vallis, D.S.; de Andrade, E.; Barcote, M.V.W.; Jurelo, A.R. Raman spectroscopy of (Fe,Li)-doped delafossite oxide CuCrO<sub>2</sub>. *Vib. Spectrosc.* **2018**, *98*, 77–81. [[CrossRef](#)]
35. Li, Z.; Deng, L.; Kinloch, I.A.; Young, R.J. Raman spectroscopy of carbon materials and their composites: Graphene, nanotubes and fibres. *Prog. Mater. Sci.* **2023**, *135*, 101089. [[CrossRef](#)]
36. Lee, M. A Raman Study of CeO<sub>2</sub> Nanomaterials with Different Morphologies. Master's Thesis, Friedrich-Alexander University Erlangen-Nürnberg, Erlangen, Germany, 2017; pp. 1–45.
37. Sakthinathan, S.; Keyan, A.K.; Rajakumaran, R.; Chen, S.-M.; Chiu, T.-W.; Dong, C.; Vinothini, S. Synthesis of N-rGO-MWCNT/CuCrO<sub>2</sub> Catalyst for the Bifunctional Application of Hydrogen Evolution Reaction and Electrochemical Detection of Bisphenol-A. *Catalysts* **2021**, *11*, 301. [[CrossRef](#)]
38. Bortamuly, R.; Konwar, G.; Boruah, P.K.; Das, M.R.; Mahanta, D.; Saikia, P. CeO<sub>2</sub>-PANI-HCl and CeO<sub>2</sub>-PANI-PTSA composites: Synthesis, characterization, and utilization as supercapacitor electrode materials. *Ionics* **2020**, *26*, 5747–5756. [[CrossRef](#)]
39. Zhang, Y.; Shi, R.; Yang, P.; Song, X.; Zhu, Y.; Ma, Q. Fabrication of electrospun porous CeO<sub>2</sub> nanofibers with large surface area for pollutants removal. *Ceram. Int.* **2016**, *42*, 14028–14035. [[CrossRef](#)]
40. Zhang, J.; Ma, Y.; Han, Y.; Xu, K.; Yao, S.; Shi, L.; Zhu, M. 3D porous structure assembled from MXene via breath figure method for electrochemical detection of dopamine. *Chem. Eng. J.* **2023**, *452*, 139414. [[CrossRef](#)]
41. Sharma, V.; Singh, P.; Kumar, A.; Gupta, N. Electrochemical detection of dopamine by using nickel supported carbon nanofibers modified screen printed electrode. *Diam. Relat. Mater.* **2023**, *133*, 109677. [[CrossRef](#)]
42. Vinoth, S.; Ramaraj, R.; Pandikumar, A. Facile synthesis of calcium stannate incorporated graphitic carbon nitride nanohybrid materials: A sensitive electrochemical sensor for determining dopamine. *Mater. Chem. Phys.* **2020**, *245*, 122743. [[CrossRef](#)]

**Disclaimer/Publisher's Note:** The statements, opinions and data contained in all publications are solely those of the individual author(s) and contributor(s) and not of MDPI and/or the editor(s). MDPI and/or the editor(s) disclaim responsibility for any injury to people or property resulting from any ideas, methods, instructions or products referred to in the content.